High-current H2+ beams from a filament-driven multicusp ion source

Massachusetts Institute of Technology

High-current $\mathbf{H_2^+}$ beams from a filament-driven multicusp ion source

D. Winklehner, J. M. Conrad, J. Smolsky, et al.

View Online   Export Citation   CrossMark

ARTICLES YOU MAY BE INTERESTED IN

High-current H_2^+ beams from a filament-driven multicusp ion source

View Online   Export Citation   CrossMark

D. Winklehner,[a)] [iD]   J. M. Conrad, [iD]   J. Smolsky, [iD]   and L. H. Waites [iD]

AFFILIATIONS

Massachusetts Institute of Technology, 77 Massachusetts Ave., Cambridge, Massachusetts 02139, USA

[a)]Author to whom correspondence should be addressed: winklehn@mit.edu

ABSTRACT

We report the results from a new multicusp ion source (MIST-1) that produces record steady-state currents of H_2^+ (1 mA) from this type of ion source with high purity (80% H_2^+). We built MIST-1 to fulfill the stringent beam purity and beam quality requirements for IsoDAR, a proposed discovery-level neutrino experiment, requiring a 10 mA, 60 MeV/amu continuous wave (cw) proton beam on the target. IsoDAR will use a cyclotron accelerating H_2^+ ions and using a novel radio frequency quadrupole (RFQ) direct injection method. Systematic measurements, varying discharge voltage, discharge current, and gas pressure, indicate that the ideal operating regime is at low pressure, high discharge current, and high discharge voltage. We have measured the combined species emittance after the source extraction to be <0.05 π-mm-mrad (rms, normalized) for a 0.95 mA beam. Beyond showing high currents and high H_2^+ fraction, our measurements agree well with high fidelity simulations. These results show the feasibility of using a multicusp ion source for IsoDAR and the RFQ direct injection prototype and paves the way to record breaking cw beam currents of 5 mA H_2^+ (equivalent to 10 mA protons) from compact cyclotrons, ideal for underground installation.

I. INTRODUCTION

In this paper, we present a significant advancement in producing continuous (DC) high-current H_2^+ beams with exceptionally low emittance and low contamination by protons and H_3^+ in a dedicated multicusp ion source. The motivation for this work lies in a novel injection and acceleration technique for compact cyclotrons. Such an accelerator that can produce 10 mA proton beams with an energy of >50 MeV and that can be mass-produced would provide a powerful tool for basic[1–3] and applied sciences.[4–6] This is an order of magnitude higher current than is available from on-market cyclotrons. It has recently been shown that the solution to many of the challenges of achieving this goal lies in accelerating 5 mA of H_2^+ ions.[3] In this paper, we report on an important first step in the development of such an accelerator: the design of the MIST-1 ion source and its commissioning at reduced power, which, nonetheless, already yielded record H_2^+ currents.

MIST-1 is an integral part of the IsoDAR project, and the requirements of this experiment have set the ion source specifications. IsoDAR is planned as a definitive search for anti-electron-flavor neutrino disappearance due to eV-scale sterile neutrinos, a beyond Standard Model particle, as described elsewhere.[1–3] The novelty of IsoDAR is in constructing an intense low energy anti-neutrino source near a kiloton scale neutrino detector, e.g., KamLAND,[7] that is located underground to reduce backgrounds (see Fig. 1). The anti-neutrinos are produced by a 10 mA, 60 MeV continuous wave (cw) proton beam impinging on a ^{9}Be target surrounded by ^{7}Li. The target is described elsewhere.[8,9] To save on space and costs, IsoDAR will use a compact cyclotron as a driver instead of a linear accelerator. Commercially available cyclotrons in this energy range typically have maximum proton beam currents around 1 mA, with space charge being the primary limiting factor. In order to reduce space-charge effects, IsoDAR will accelerate H_2^+ instead of protons or H^- (note that we also investigated H_3^+, but the higher rigidity would make the cyclotron larger and more expensive). With this, and additional innovations described in Ref. 3 (axial injection through an radio frequency quadrupole (RFQ), high accelerating gradient, and vortex motion), the IsoDAR cyclotron will accelerate 5 mA of H_2^+ to 60 MeV/amu, which, after charge-stripping, yields 10 mA of protons at 60 MeV on the target.
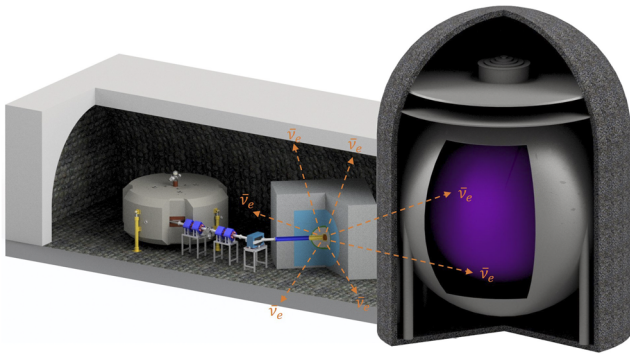
FIG. 1. Artist's rendition of the IsoDAR experiment paired with the KamLAND detector at Kamioka. From left to right: The cyclotron (ion source on the top), generating a 60 MeV/amu H_2^+ beam, the medium energy beam transport line, the neutrino production target, and the KamLAND detector.

The ion source requirements for RFQ direct axial injection into the compact cyclotron are

1. low emittance ($< 0.1 \pi$-mm-mrad, rms, normalized),
2. low contamination ($> 80\%$ H_2^+ fraction),
3. high current (10 mA of H_2^+), and
4. DC mode (i.e., non-pulsed, non-bunched).

These stem from the desire to keep the system compact and utilize the RFQ's ability to separate by mass in addition to its highly efficient bunching and pre-acceleration. In Fig. 1, the entire low energy beam transport (LEBT) is contained within the six-way cross on top of the cyclotron.

The status of high current H_2^+ and H_3^+ sources was recently reviewed in Ref. 10, which lists 2.45 GHz Electron Cyclotron Resonance (ECR) ion sources[11,12] and filament-driven discharge sources, with the plasma either confined by a solenoid[13] or by a multicusp field.[14] For IsoDAR, we tested the 2.45 GHz ECR versatile ion source (VIS)[15,16] first in collaboration with INFN-LNS and Best Cyclotron Systems, Inc. While the performance for protons was excellent, we found that the maximum H_2^+ fraction was limited to 50% at the required total beam currents.[17,18] In Ref. 10, similar fractions are reported. In Ref. 19, a filament discharge source with solenoid confinement was presented that showed >91 % H_2^+ fraction and 2.84 mA of H_2^+; however, the energy spread was on the order of 120 eV (reported for a He^+ beam). In Ref. 14, a multicusp ion source, developed at LBNL, capable of producing extractable total current densities of 50 mA/cm^2, with up to 80% of the beam being H_2^+ ions, was presented. Combined with typically low emittances (e.g., <0.04 π-mm-mrad for Ar^{+}[20]), low energy spread (< 2 eV[21]), and ease of operation, we deemed this type the best choice for a new source. It is important to note that the LBNL source was never intended to provide the beam to an experiment, and thus, the average beam power was orders of magnitude lower than what we need. A current density of 50 mA/cm^2 was obtained with a Langmuir probe, and the highest extracted current reported is only 0.32 mA. Furthermore, the source seems to have been operated in pulsed mode. To fulfill the IsoDAR requirements, we designed MIST-1 to deliver 10 mA of H_2^+ beam current in DC mode, which required significant design changes and cooling upgrades.

In this early commissioning phase, MIST-1 has already set a new record for this type of ion source: a 1.08 mA DC H_2^+ beam. At full power, MIST-1 must deliver a 10 mA DC H_2^+ beam to the RFQ and cyclotron. With a demonstrated current density of 11 mA/cm^2 and doubling the aperture size from 4 to 8 mm diameter, the scaled H_2^+ current of 4 mA H_2^+, when run through our detailed cyclotron simulations, would already allow building a compact cyclotron that can deliver four times the current of a commercial system. Additional development is ongoing that will bring us to the nominal current of 10 mA H_2^+. In addition to the beam currents, we show that simulations of very low initial emittances (<0.05 π-mm-mrad rms, normalized) are in good agreement with measurements. Section II contains a detailed description of the source and diagnostic setup. Section III covers simulations of the extraction system and test beamline. Measurements are shown in Sec. IV.

II. EXPERIMENTAL SETUP

A. Ion source

The MIST-1 ion source is a filament-driven multicusp ion source and is described in detail in Refs. 2, 3, and 22. A computer aided design (CAD) rendering is shown in Fig. 2, and a cross section view is shown in Fig. 3 (right). A stainless steel chamber with samarium–cobalt permanent magnets creates a multicusp field that confines the plasma around the extraction aperture. Hydrogen enters the source through the back plate. The hydrogen undergoes electron-impact ionization by electrons from the tungsten filament, which are being accelerated toward the anode. The filament is a tungsten alloy, mixed with small amounts of copper and nickel for corrosion resistance. The ions are then extracted through a hole in the center of the front plate. The source is on a high voltage platform that can be lifted to a maximum potential of 20 kV. Ions leaving the source are focused and accelerated in the extraction system. The ion source parameters described here are summarized in Table I.

The amount of hydrogen entering the source is controlled by using a mass flow controller (MFC) (MKS Instruments, Model: GV50A, with 5 SCCM full range). The MFC is controlled via
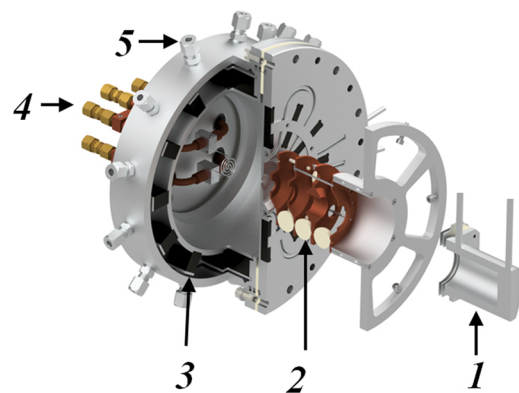

FIG. 2. 3D CAD rendering of the MIST-1 ion source with the extraction system and Faraday cup 1 (FC1). Inner parts are labeled: (1) Faraday cup, (2) extraction system, (3) permanent magnets (Sm_2Co_{17}), (4) water cooled filament feedthroughs, and (5) water cooling fittings. The back plate also has a gas inlet, through which the hydrogen gas may enter into the source.
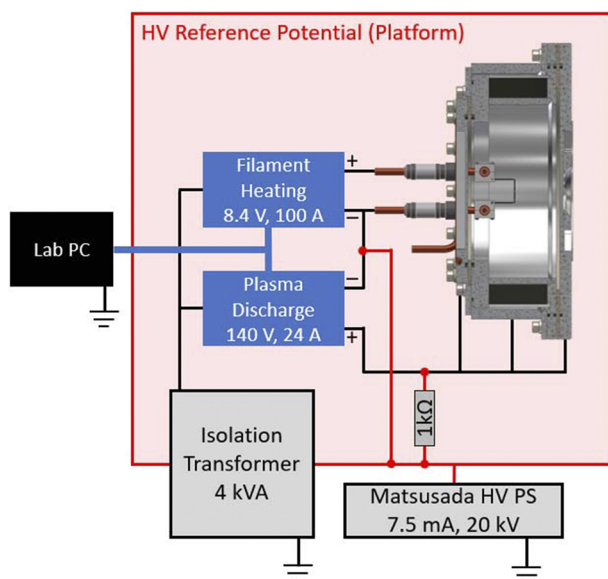
FIG. 3. The wiring schematic of the ion source. Red represents the high voltage reference potential, blue represents the data cables, and black represents the power cables. The power supplies are computer-controlled via an optical USB extender cable. The source back plate, body, and front plate can all be held at different potentials (they are separated by insulator rings). During the measurements presented here, they were held at the same potential.

TABLE I. MIST-1 ion source parameters.

Parameter	Value (nominal)
Plasma chamber length	6.5 cm
Plasma chamber diameter	15 cm
Permanent magnet material	Sm_2Co_{17}
Permanent magnet strength	1.05 T on surface
Front plate magnets	12 bars (star shape)
Radial magnets	12 bars
Back plate magnets	Four rows of magnets, six bars tot.
Front plate cooling	Embedded steel tube
Back plate cooling	Embedded copper pipe
Chamber cooling	Water jacket
Water flow (total)	≈2 l/min
Filament feedthrough cooling	Water cooled
Filament material	Water mixed with Cu and Ni
Filament diameter	≈0.8 mm
Discharge voltage	Max. 180 V
Discharge current	Max. 24 A
Filament heating voltage	Max. 8 V
Filament heating current	Max. 100 A

an RS485/USB optical extender connected to our control system personal computer (PC).

The filament is connected to two power supplies (see Fig. 3): The filament heating power supply (8.4 V, 300 A max), to raise the temperature of the filament for thermionic electron emission, and

the plasma discharge power supply (150 V, 24 A max), to maintain a potential difference between the filament (cathode) and the source body (anode), facilitating discharge. The source body, back plate, and front plate are all electrically insulated. This will allow us to put each component at a different potential in order to test the effects of varying the anode arrangements in future studies. Note that the wiring in Fig. 3, while being slightly more flexible in terms of cathode–anode arrangements, has the drawback of changing the ion energy (here, $V_{source} \cdot e + V_{dis.} \cdot e + V_{plasma} \cdot e$ with e being the elementary charge) when changing $V_{dis.}$. We have factored this into the analysis. For final deployment, we will have the control system automatically adjust V_{source} for changes in $V_{dis.}$. For this study, we maintained all components at the same potential. The filament emits electrons that ionize the gas to form a plasma. H_2^+ is a fragile ion that easily recombines to H_3^+ in collisions with H_2 or dissociates into protons through further collisions with plasma electrons. We estimated the mean free path for collisions of H_2^+ with neutral H_2 in MIST-1 to be between 5 and 20 cm, depending on the gas flow (cf. Sec. IV D). We account for this with a short source body (low aspect ratio), producing the bulk of H_2^+ within a few centimeters of the extraction aperture. The short source body could also have the added beneficial effect of primary electrons being lost to the source front plate before they lose much of their energy through collisions, shifting the electron energy distribution (EED) in the plasma toward higher energies (end point at discharge voltage + plasma potential). As was pointed out elsewhere,[23] higher electron energies favor excitation to singlet states over triplet states (which are predominantly from electron collisions below 20 eV). Triplet states feed the H^+ and H_3^+ fractions by creating free H.[24] Having predominantly singlet excited states, thus, benefits H_2^+ production.

The size, shape, and position of the filament have an effect on the properties of the plasma. We have found that using a filament that is less than 0.8 mm thick does not provide sufficient electrons to generate a dense plasma. A systematic study for optimal filament shape, thickness, and position is forthcoming. The specific parameters of each filament used in the studies presented here will be described in Sec. IV.

The ions drift out of the source through the extraction aperture where they are shaped and accelerated by a pentode extraction system. The extraction system is a series of four copper electrodes that shapes the beam on leaving the ion source (see Fig. 6) through static voltages applied by Matsusada power supplies AU-20P7 and AU-20N7, for positive and negative voltages, respectively. The electrodes following the source plate are the screening electrode, or "puller" (typically kept at a low, negative voltage of −2 kV), and the einzel lens. The puller prevents electrons from the beamline from streaming back into the ion source and increases the electric field that shapes the meniscus. The einzel lens is made up of a total of three electrodes. The outer ones are grounded, and the larger central piece is adjustable up to 20 kV. This feature is mostly unused in the presented measurements. The electrodes are aligned via the compression of several ceramic balls. The extraction system is modeled using the IBSimu code,[25] as discussed in Sec. III.

B. Low energy beam transport and diagnostics

The ion source extraction system is followed by a low energy beam transport (LEBT) line used for beam diagnostics. The LEBT

TABLE II. Parameters for the beamline magnets.

Dipole parameter	Value	Quad parameter	Value
Manufacturer	Bruker	Manufacturer	BNIP
B_{max} (center)	0.7 T	B_{max} (pole tip)	0.085 T
I_{max}	125 A	I_{max}	200 A
U_{max}	47 V	U_{max}	2 V
Bending radius	300 mm	Pole tip radius	37.5 mm
Pole gap	75 mm	Aperture diameter	90 mm

consists of three electromagnets: two quadrupole magnets (Q1, Q2) and one dipole magnet (D1). The arrangement of the magnets, beamline, and diagnostics six-way crosses (designated as DB1 and DB2 in the text below) are shown in Fig. 4. Parameters for the magnets are listed in Table II. Both the quadrupole magnets can be used for vertical focusing of the beam; however, only Q1 is used for the studies presented here. When we take a mass spectrum, the current in Q1 is increased in a constant ratio with the current in D1. The dipole magnet is used for horizontal focusing and ion species separation. Following Q2 is the analysis six-way cross (DB2), which contains a second Faraday cup and two Allison scanners with perpendicular axes.

The Faraday cup (FC1) in DB1, which follows the extraction system, is used to measure the total current coming from the source without the separation of species. A second Faraday cup (FC2) is located at the end of the beamline to measure the relative species fractions after separation by the dipole (see Fig. 5). Each Faraday cup is equipped with a negative suppression electrode to prevent secondary electrons from escaping, which would artificially increase the measured positive ion current. The necessary suppression voltage for our Faraday cups has been experimentally determined to be −350 V.

To measure horizontal and vertical emittance (separately), DB2 houses two Allison-type electrostatic emittance scanners.[26] A model for the identical Allison scanners, designed and constructed at the MIT, is shown in Fig. 5. They are equipped with a water-cooled copper front plate and are able to handle proton beam currents of up to 50 mA and 80 keV. Further details are provided in Ref. 27.
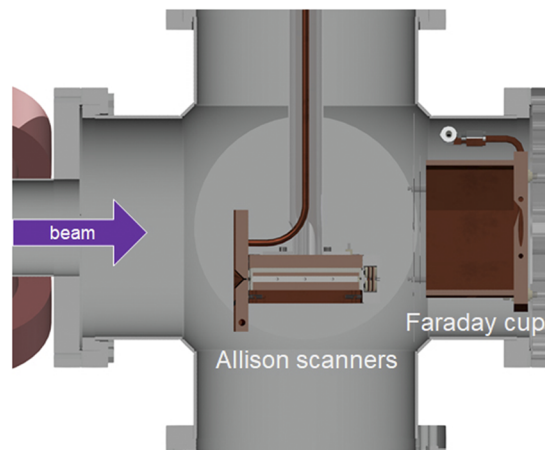

FIG. 5. CAD rendering of DB2, housing the Allison scanners (vertical scanner shown) and FC2. The Allison scanners can be retracted so that the beam current can be measured in FC2 to obtain mass spectra.

C. Measurement parameters

We are doing systematic studies during commissioning of this source by varying the following parameters:

- discharge voltage,
- filament heating current,
- H_2 gas flow into the source, and
- filament shape and position.

The filament shape and position can only be adjusted when the source is opened, and we will study them further in future work. We set the H_2 gas flow several hours before measurements to allow ample time for the vacuum system to reach the steady state.

The filament discharge current typically strongly affects the plasma density and can oscillate with filament temperature changes and pressure fluctuations. We use the filament heating current to compensate for these fluctuations and to keep the discharge stable. This is controlled by a proportional–integral–derivative control loop, or "PID loop,"[28] which acts on a time scale of 0.1 s. As we vary
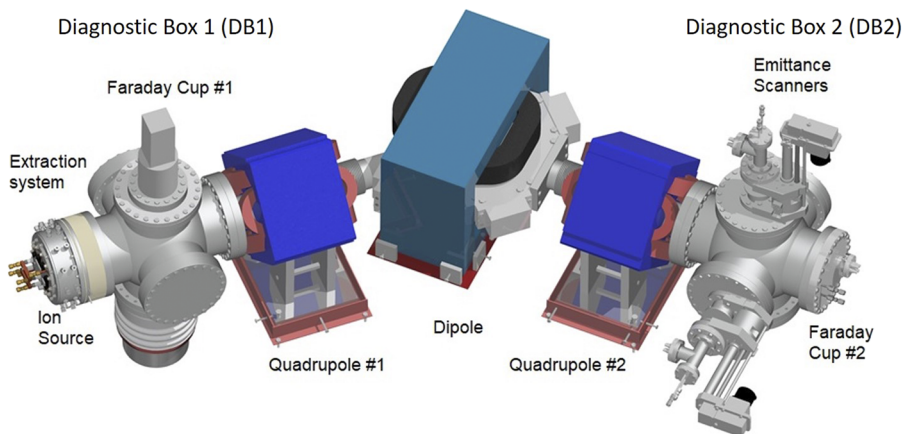

FIG. 4. CAD model of the LEBT and diagnostic system. Starting with multiple species coming from the ion source, the species are then focused on the beamline by quadrupole magnets and separated by the dipole magnet. Their currents and emittances can then be measured by using the Faraday cup and emittance scanners in DB2.

the main measurement parameters (gas flow, filament heating current, and discharge voltage), we measure the total current in FC1. As the changes in plasma density influence focusing at the plasma aperture ("plasma meniscus"), we adjust the platform voltage to keep the beam focused into FC1, which is monitored by measuring the current on its front plate. In this measurement period, we kept the puller voltage constant at −2 kV, but in the future, this can also become a knob to adjust the plasma meniscus.

Before an ion mass spectrum, further focusing is done with a single species (typically H_2^+) focused into FC2 using the dipole magnet. The einzel lens voltage and Q1 current are then varied while monitoring the transmitted current in FC2. This determines the fixed einzel lens value and the constant of proportionality between D1 and Q1 we use in the measurement.

When recording a mass spectrum, we vary the current in D1 while measuring the beam current in FC2. We set the current in Q1 proportional to D1, which gives, to first order, identical focusing of the various species (neglecting changes in space-charge compensation). FC2 currents are then plotted as a function of dipole field (see Sec. IV). As ions with different mass-to-charge ratios have different magnetic rigidities, a different D1 field strength is necessary to transport them to FC2, thus leading to individual peaks in the spectrum. The magnets are controlled, and mass spectra are recorded via an automated LabVIEW program run on a PC.

III. SIMULATIONS

We simulate the extraction from MIST-1 and the subsequent beam transport using two publicly available software packages: IBSimu[25] and Warp.[29,30] IBSimu is used initially because it accurately models ions traversing the plasma sheath. However, IBSimu would be too computationally expensive to use for a simulation of the entire test beamline. On the other hand, Warp accurately models space-charge effects and beam transport, with less computing power than IBSimu, but the plasma sheath modeling in Warp is not well-established. This led to the decision to combine the packages in series. We use IBSimu to simulate the ions from the ion source to midway through the first six-way cross, and we then use Warp from the first six-way cross to the end of the beamline.

A. Ion source extraction (IBSimu)

We designed and simulated the extraction system using IBSimu, a particle-in-cell code developed at Jyväskylä, which uses iterative processes to calculate the particle trajectories through electromagnetic fields. IBSimu has successfully been used to design and simulate several extraction systems and is well-benchmarked against experimental results.[31–34] IBSimu uses electrode geometries that are imported from CAD files. The electrodes, set to static potentials, are then used to calculate the external fields in the system. The particle trajectories are simulated by ray-tracing of the particles through the superposition of the external field and the beam's self-field (space charge). This process is repeated until the simulation converges. Multiple species can be simulated simultaneously, accounting for the space-charge effects of each. IBSimu is used for the first 14 cm of the beamline. As an example of a typical IBSimu simulation of MIST-1, we show the particle trajectories in Fig. 6. Here, we did not use the einzel lens.
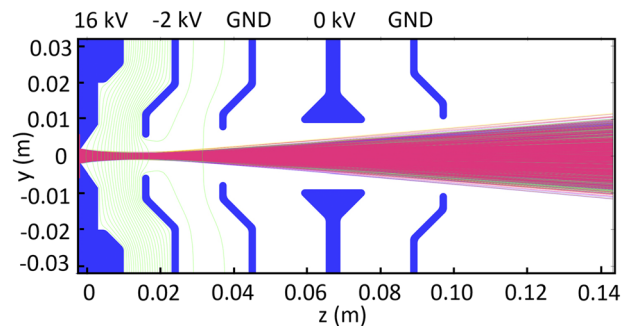

FIG. 6. IBSimu simulation of the low energy extraction system. The electrodes are shown in blue, and the equipotential lines are shown in green. The electrode voltages are shown at the top. This simulation includes all species listed in the text.

B. Low energy beam transport (Warp)

Warp is a particle-in-cell Python package that has been developed since the 1980s at Lawrence Livermore National Laboratory and Lawrence Berkeley National Laboratory.[29,30] The particle distributions from IBSimu simulations are loaded as the initial distributions for the Warp simulations. Particles are propagated using the wxy-slice package. The wxy-slice package calculates the transverse space-charge effects at each step, but ignores longitudinal space-charge effects, which is a good approximation for slow-changing DC beams, and brings significant simulation speed-up. Space-charge compensation (from residual gas ionization in regions free from electrostatic fields) is treated as a free parameter and simulated by modifying each species' current: $I_{comp} = I_i \cdot (1 - f_e)$ with f_e being the space-charge compensation factor from the literature.[35] A more accurate space-charge compensation model will be implemented in future simulations.[36] Simulations are done for the entire beamline and individual sets of parameters, matching emittance measurements and mass spectrometer measurements.

Included in the simulations are models of the magnetic fields and vacuum components. In order to accurately model the quadrupole and dipole magnets, CAD models of the yokes and coils were imported to COMSOL[37] to calculate 3D fields using finite element methods. These fields are imported into Warp with a scaling factor to simulate different field strengths. Vacuum components are accounted for by using Warp's internal functions to generate conductor data from Boolean operations on primitive shapes. Conducting cylinders are used for the vacuum tubes and six-way crosses; a rectangular box is used for the dipole chamber. Particles coming into contact with conductors are removed from the simulation and the currents are adjusted after each simulation step.

At the beginning of the Warp simulations, the beam has a circular cross section and nearly identical phase spaces for xx' and yy'. During simulations, the maximum and two-rms beam envelopes are saved at each step, and the phase space of all remaining particles is saved at the end of each simulation (see Fig. 7 for a typical output plot). To determine the beam composition (species and currents) for the simulations, mass spectrum measurements were used. Since the electrostatic elements focus all species in the same way and the quadrupole current is scaled with the dipole current during each spectrum, to first order (neglecting any space-charge compensation changes), the measured spectra are representative of the
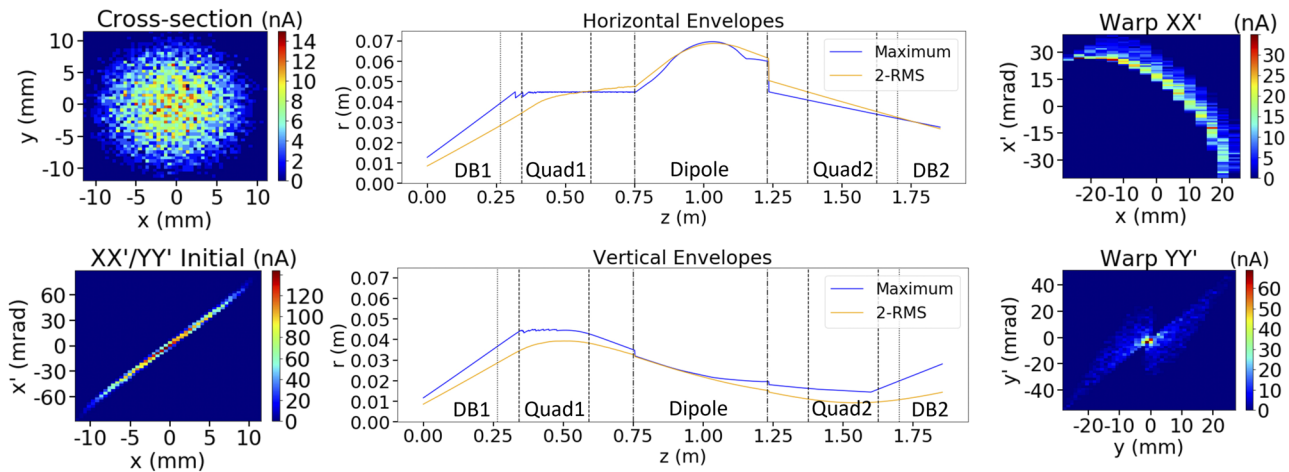
FIG. 7. Example simulation of the test beamline using Warp. The simulation starts 14 cm from the extraction aperture. The left plots show the initial cross section and phase space. The middle plots show the maximum and two-rms envelopes for H_2^+. The vertical lines show the boundaries of the diagnostic boxes and magnets. The right plots are the phase spaces at the end of the simulation.

initial species ratio. By varying the dipole scaling factor in Warp, the current measured in FC2 during an actual dipole sweep can be simulated. Good mass separation is achieved by placing a 1 cm wide slit between the dipole magnet and FC2 in the experiment and in the simulations. Emittance scans can be matched at the z position of the Allison scanners by creating a 2D histogram of the simulated particle phase spaces in the same location.

The simulated dipole scans show good quantitative agreement with measured spectra. The simulated phase spaces show excellent qualitative and good quantitative agreement with emittance scans using the Allison scanners. As an example, we used typical experimental settings in the described simulation deck, and the results are plotted in Fig. 7. The species considered in these simulations are H^+, H_2^+, and H_3^+, with small contributions from N^+, O^+, H_2O^+, N_2^+, and O_2^+. We obtained the ratios from the corresponding measured mass spectrum. The higher mass ions are on the order of a few percent

due to insufficient pumping time in this case (air containing water vapor can get into the source chamber during a filament change). Minimal contamination with F^+ and HF^+ (a few percent) can also occur due to outgassing of a fresh Viton O-ring before "baking" the source.

The total current from the source was 850 μA, and the H_2^+ current arriving at the scanner location was 200 μA. The space-charge compensation factor f_e was set to 0.74 to reach the best agreement between simulation and measurement. The simulated rms, normalized emittances at the end of the beamline were 0.44 π-mm-mrad and 0.28 π-mm-mrad for the horizontal and vertical scans, respectively. The large emittance growth can be attributed to aberrations and fringe fields of the magnets, and space charge. Simulations show continuous emittance growth in the LEBT until the exit of the dipole chamber, which acts as a collimator. The emittance growth and particle loss for H_2^+ in the LEBT are shown in Fig. 8.
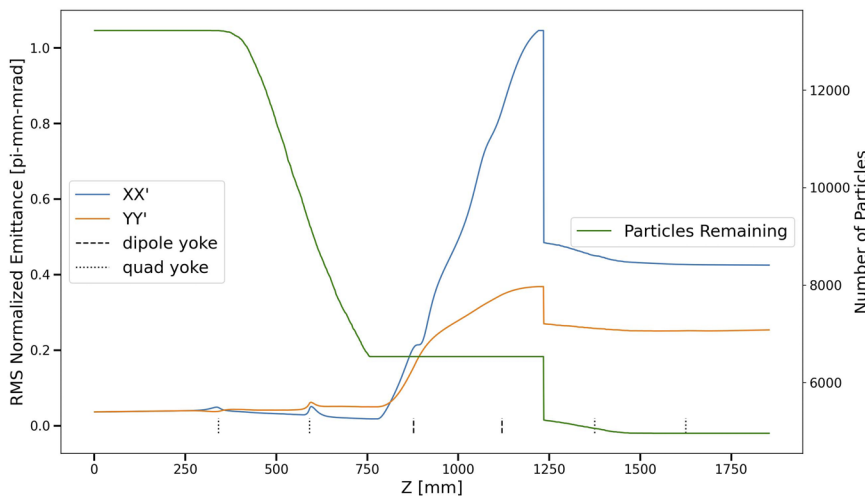

FIG. 8. Emittance growth and particle loss in the LEBT. The vertical black lines indicate the edges of the electromagnet yokes. Halo particles removed by terminating on the beam pipe slow the emittance growth until the beam reaches the dipole chamber (which extends beyond the dipole yoke on both the ends). The emittance grows rapidly within the dipole chamber. The sudden drop in emittances and particle number occurs at the end of the dipole vacuum chamber where the beam enters the beam pipe again.

IV. MEASUREMENTS

In this section, we present first measurements of ion species ratios from the MIST-1 ion source. This establishes the base level of performance for this device, which can be further tuned as needed for future applications. Note that the ion source front plate has an exchangeable disk that lets us use different extraction aperture diameters. During the presented measurements, we used two diameters, 3 and 4 mm; hence, currents are also reported as densities in mA/cm^2.

In all systematic parameter variations, we see some small contamination, most likely from outgassing of Viton O-rings (H_2O^+, F^+, and HF^+). These are on the order of a few percent and lumped together as "Other" in the plots.

The results are discussed in Sec. IV D.

A. Performance tests

The first results we report here are of the ion source peak performance to date: The highest extracted current density, the highest H_2^+ fraction, and the highest total extracted H_2^+ current density (a balance between the H_2^+ fraction and the total extracted current density).

Highest total current. With 5.2 mA of the total beam current measured in FC1, the highest current density we recorded so far was ≈ 41.4 mA/cm^2 (4 mm diameter aperture). This was with a discharge voltage of 150 V, a discharge current of 10.8 A, and a H_2 flow of 1.3 SCCM. Accordingly (see discussion below), the species balance was shifted toward H_3^+, with an H_2^+ fraction of $\approx 31\%$ and H_3^+ fraction of $\approx 42\%$. This corresponds to an H_2^+ current of 1.6 mA out of the source, albeit not at the required 80% purity.

Highest H_2^+ contribution. With a lower H_2 flow of 0.275 SCCM, $V_{discharge} = 125$ V, and $I_{discharge} = 7$ A, the highest fraction of H_2^+ was recorded as 76%. The total extracted current was 1.42 mA (11.4 mA/cm^2). The corresponding mass spectrum is shown in Fig. 9. We saw 470 μA of H_2^+ in FC2 at the end of the beamline, constituting a beamline transmission efficiency of 44%, which agrees with simulations.

Highest total H_2^+ current density. With a H_2 flow of 0.375 SCCM, $V_{discharge} = 110$ V, and $I_{discharge} = 9$ A, we recorded a H_2^+ fraction of 62% at a total ex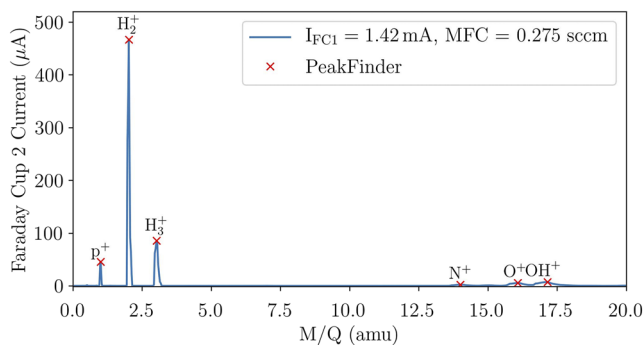tracted current of 2.1 mA. This corresponds to an H_2^+ current density of 10.4 mA/cm^2 (1.3 mA). This is the highest current we recorded with H_2^+ being the dominant species.

B. Systematic parameter variations

The ion source is designed to allow several parameters to be varied. Here, we provide information on the total current and species composition of the beam for variations of the hydrogen gas flow, discharge voltage, and discharge current.

Hydrogen flow. In the first series (see Fig. 10), the discharge current was held stable at 4 A via the PID loop. The mass flow was varied from 0.25 to 1.25 SCCM. As the mass flow is increased, the total extracted current rises from 0.5 to 2.12 mA. To compensate for changes in the plasma meniscus, the source voltage was raised (from 10 to 13 kV) in concert with the total extracted current to focus the beam into FC1 (i.e., no observable current on the grounded Faraday cup front plate). This procedure should not influence the ratio of species measured in FC2, as the electrostatic elements focus all masses the same and the magnetic elements (Q1 and D1) are ramped together. While the overall transmission can change between measurements, it does so for all species. Notably, the H_2^+ contribution rises toward the lower gas flow rate, while H_3^+ rises toward the higher gas flow rate. Throughout all of our measurements, we observed an optimal mass flow for H_2^+ production between 0.15 and 0.25 SCCM.

In a second series (see Fig. 11), we varied the gas flow and reduced the discharge current in parallel (by reducing the filament heating current and, thus, the number of primary electrons) to keep the total current in FC1 constant at 1.25 mA. Here, we held the source voltage at 10 kV not affecting any changes in beamline transmission during the measurement. We observe a behavior similar to that in the first series.

Discharge voltage (see Fig. 12). Here, we varied the discharge voltage from 50 to 150 V, while keeping the H_2 flow rate constant at 0.375 SCCM. We kept the filament discharge current constant at 4 A via the PID loop. The total extracted current changes slightly in this mode, but not significantly enough to necessitate changes in source voltage or tuning of the LEBT. We observe no strong dependency of species ratios in this regime.
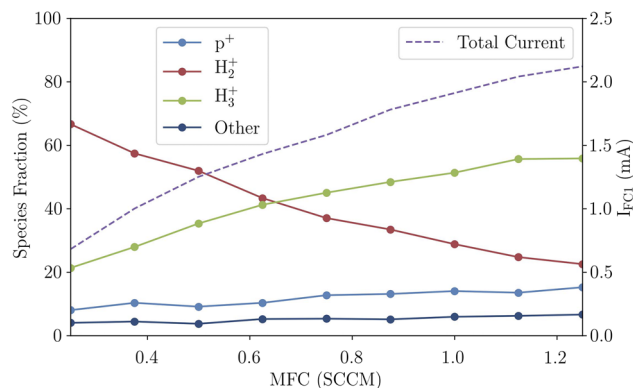
FIG. 9. Mass spectrum for the H_2 flow = 0.275 SCCM and 125 V discharge voltage. The H_2^+ fraction is 76%.

FIG. 10. Variation of the hydrogen flow from the MFC, while keeping the discharge current constant at 4 A. We observe the typical trend of increasing H_3^+ and decreasing H_2^+ with a high mass flow.
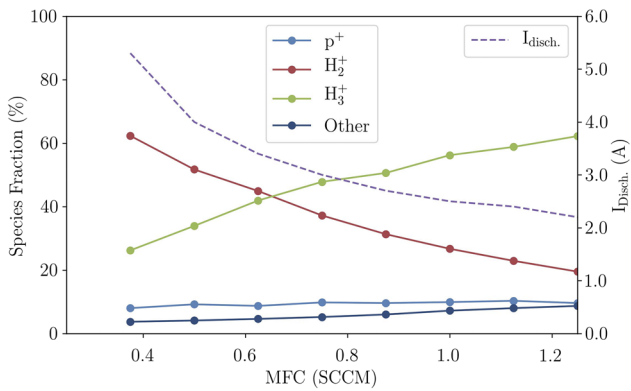
FIG. 11. Variation of the hydrogen flow from the MFC, while keeping the total extracted current constant at 1.25 mA by decreasing the filament heating current. We observe the typical trend of increasing H_3^+ and decreasing H_2^+ with a high mass flow. Note that for the lowest gas flow (0.25 SCCM), we could not reach 1.25 mA as we reached the voltage limit of the filament heating power supply. Thus, this data point is omitted.
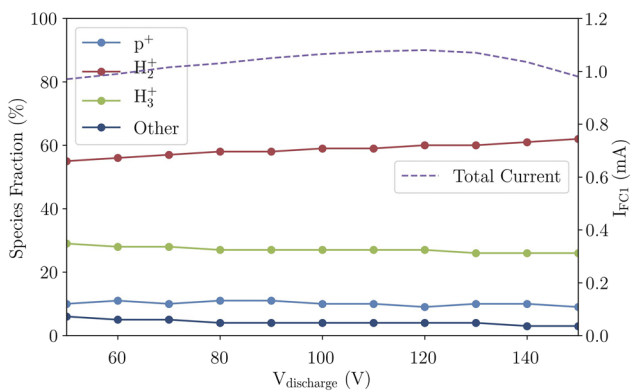

FIG. 12. Variation of discharge voltage. Here, we kept the discharge current constant at 4 A and the H_2 flow at 0.375 SCCM. We observe no strong dependency of species ratios in this regime.

Discharge current (see Fig. 13). Here, we varied the discharge current from 2 to 8 A, while keeping the H_2 flow rate constant at 0.375 SCCM and the discharge voltage at 150 V. While increasing the discharge current, the total extracted current increased almost linearly. To compensate for changes in the plasma meniscus, the source voltage was raised in concert with the total extracted current to focus the beam into FC1 (i.e., no observable current on the grounded front plate). We observe no strong dependency of species ratios in this regime.

C. Emittance measurements

To confirm the low emittances from the literature and from our IBSimu simulations, we first measured the combined emittance of all ion species using the vertical emittance scanner in the location of FC1 in DB1. Here, all singly charged ions are focused the same way in the extraction system, and to first order, the combined emittance
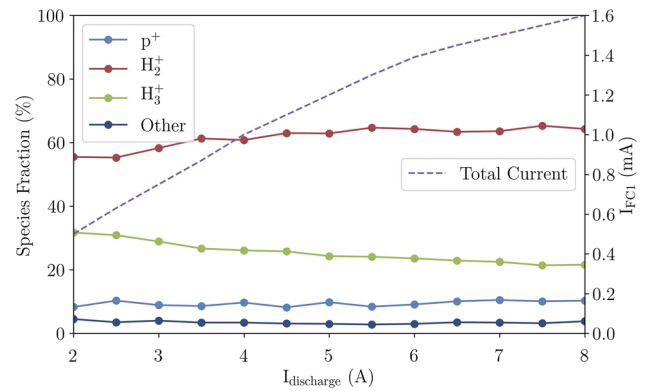

FIG. 13. Variation of discharge current. Here, we kept the discharge voltage constant at 150 V and the H_2 flow at 0.375 SCCM. We observe no strong dependency of species ratios in this regime.

corresponds to the emittance of a pure H_2^+ beam with the corresponding total current. This does not take into account the effect of space-charge compensation, which is small over this short distance. We used a mass flow of 0.25 SCCM and $V_{dis.} = 150$ V to obtain a

TABLE III. Measured rms, normalized vertical emittances of the beam before mass separation (in DB1 at the location of FC1).

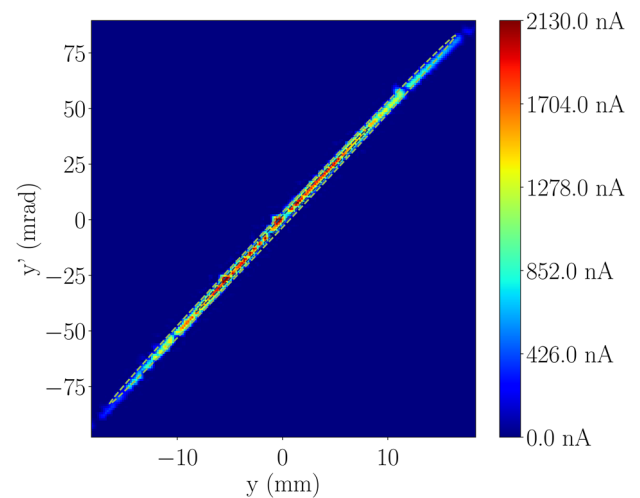| $I_{dis.}$	I_{total} (mA)	$\varepsilon_{y,rms,norm.}$ (π-mm-mrad)
1 A	0.30	0.033
2 A	0.68	0.046
3 A	0.73	0.048
4 A	0.95	0.046

FIG. 14. Example vertical emittance scan at the location of FC1 in DB1. The rms emittance is 0.046 π-mm-mrad for a total beam current of 0.95 mA (73% H_2^+). The source and einzel lens voltages from previous measurements (best LEBT transmission) were used for consistency, and the beam was not tuned for minimum emittance at this location.

high H_2^+ fraction (> 70%). We used V_{source} = 10 kV and $V_{Einzel\ Lens}$ = 8 kV to be consistent with the measurements presented in Sec. IV B (tuned for LEBT transmission and not for minimum emittance). The resulting rms, normalized vertical emittances for several different discharge currents are listed in Table III and are below 0.05 π-mm-mrad, as expected. At this position, and with these settings, the beam is close to a Kapchinsky–Vladimirsky distribution, and the four-rms emittance contains 99% of the beam. An example can be seen in Fig. 14, which can be compared to Fig. 7 (lower left) although the two plots are at different longitudinal positions along the beamline.

We then measured horizontal and vertical emittances of mass-separated H_2^+ in DB2. An example of the results from the two Allison emittance scanners can be seen in Fig. 15, for a mass-separated H_2^+ beam. The total current from the source was 850 μA, and the H_2^+ current arriving at the scanner location was 200 μA. Simulating the beamline with the same parameters allows a demonstration of good qualitative and quantitative agreement with the IBSimu/Warp simulation of the setup (cf. Sec. III). The measured rms, normalized emittances at the end of the beamline were 0.37 π-mm-mrad and

TABLE IV. Measured and simulated beam parameters for the MIST-1 diagnostic beamline. Measured in DB2.

Parameter	Measured	Simulated
$\varepsilon_{x,rms}$ (mm-mrad)	0.37	0.44
$\varepsilon_{y,rms}$ (mm-mrad)	0.28	0.28
Diameter$_{x,rms}$ (mm)	8.9	8.8
Diameter$_{y,rms}$ (mm)	35.2	35.4
Transmission (%)	29.4	30.3

0.28 π-mm-mrad for the horizontal and vertical scans, respectively. A comparison of measured and simulated values can be found in Table IV. In the phase spaces of Fig. 15 (top and bottom), the same features can be seen.

D. Discussion

Within the tested limits, only the variation of the gas flow, and, thus, the pressure inside the ion source, had a strong impact on the
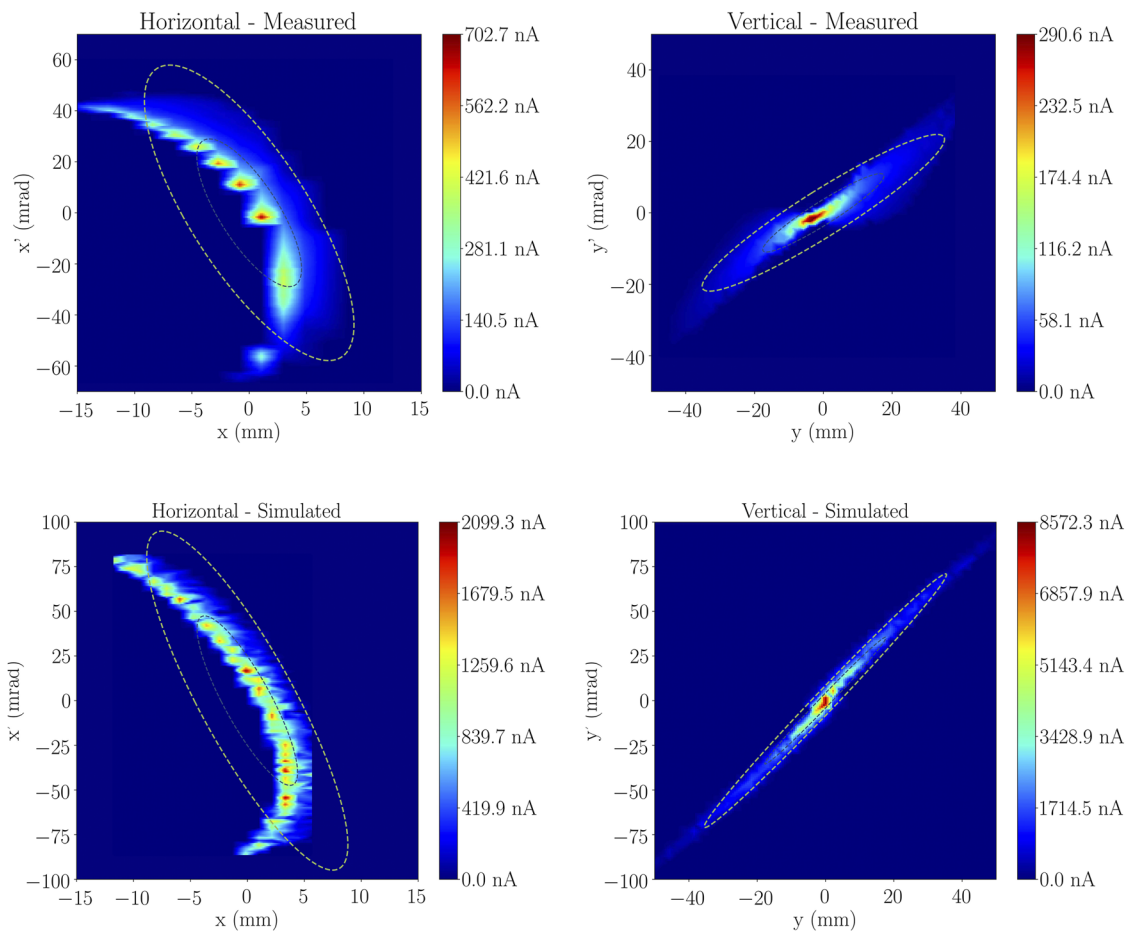

FIG. 15. (Top) First emittance scans of a mass-separated H_2^+ beam. (Bottom) Corresponding simulation results. Good qualitative agreement was found with Warp simulations. The rms values and transmission also agree well (see Table IV).

ion species distribution. As the proton fraction does not significantly change, to first order, we attribute the behavior to collisions of the H_2^+ ions with neutral H_2 molecules,

$$H_2^+ + H_2 \rightarrow H_3^+ + H.$$
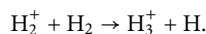
Following Ehlers and Leung,[14] we estimated the mean free path $\lambda = 1/(n_0\sigma)$ of this reaction to be between 5 and 20 cm depending on the gas flow into the source (see Fig. 16). We obtained the cross section ($\sigma \approx 3 \cdot 10^{-15}$ cm^2) for this process from IAEA's ALADDIN database,[38] assuming 1 eV of projectile (H_2^+) energy and a gas pressure between $5 \cdot 10^{-4}$ and $2 \cdot 10^{-3}$ Torr inside the source. We estimated the temperature to be 50–60 °C, identical to source body and back plate temperatures.

Furthermore, we observe that increasing gas flow and increasing $I_{discharge}$ (by increasing filament heating) both increase the total current measured in FC1. The latter is not surprising as higher discharge current typically means more primary electrons are available to ionize H_2. When increasing the gas flow, $I_{discharge}$ (if not restricted) rises quickly, together with the total extracted current (not shown). In the first reported measurement (see Fig. 10), we restrict the discharge current to 4 A with the help of the PID loop, which regulates down the filament heating. However, the total extracted current still increases. In the second series of the pressure variations (see Fig. 11), we reduce the discharge current (by decreasing filament heating) to keep the total beam current constant. Thus, it is immediately clear that the discharge current is not a direct measure of the plasma density as both primary electron number and neutral gas density have a strong influence on the plasma density and extracted current. Indeed, the discharge current is the sum of negative charges leaving the filament (primary electrons) and hitting the source chamber and positive charges either sputtered off the source chamber or hitting the filament. In addition, the EED could be modified through the various collision processes in the plasma and influence the aforementioned excitations to singlet and triplet states.

We are working on a more complete model of the plasma, incorporating rate equations of the processes involved[39] (cf. also Fig. 17) and a better estimate of the electron energy distribution
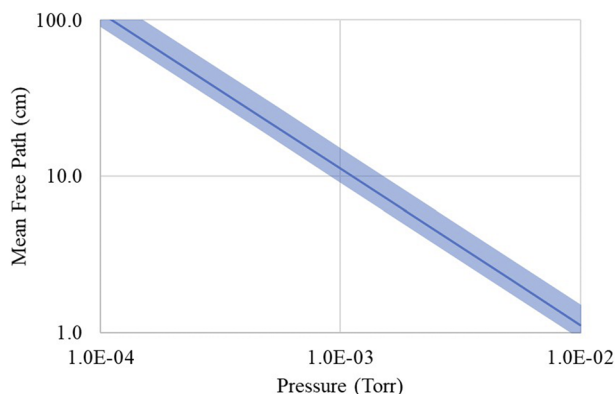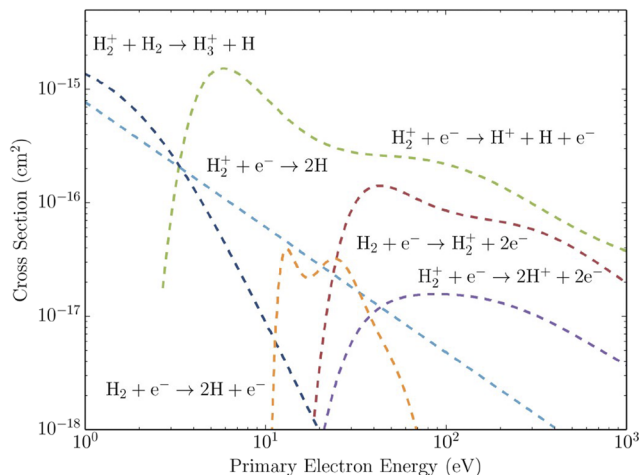

FIG. 17. Reaction cross section for processes involved in the production, recombination, and dissociation of H_2^+. In the case of $H_2^+ + H_2 \rightarrow H_3^+ + H$, *primary energy* refers to H_2^+, in all other cases to electrons. Reproduced with permission from S. Axani, Proc. Sci. **282**, 484 (2017). Copyright 2017; Author(s), licensed under a Creative Commons Attribution 4.0 License.

(EED) and electron, neutral, and ion densities. Understanding the EED and excitation rates to singlet and triplet states[23] will give valuable insights and possibly let us explain also the more subtle changes in H_2^+ and H_3^+ fractions in Figs. 12 and 13. We are also planning to add plasma diagnostics to our ion source. This is a work in progress, however, and goes beyond the scope of this paper, which is reporting commissioning results at high current with a high H_2^+ fraction in DC mode.

So far, our measurements indicate that H_2^+ becomes the dominant species at a low H_2 mass flow (0.25 SCCM and below), and high $V_{discharge}$ and $I_{discharge}$ contribute further. This is also in agreement with earlier findings by Ehlers and Leung[14] and Lee *et al.*[21]

In the next measurement period, the filament position will be varied to find the maximum extracted current with a high H_2^+ fraction. Other planned improvements to the source include better water cooling and a plasma aperture made from a tungsten alloy (75% W, 25% Cu) to improve heat transfer away from the source aperture and to provide better thermal stability.

The quality (emittance) of the beam extracted from the ion source is very good, as is typical for filament-driven multicusp ion sources, and we measured normalized rms emittances below 0.05 π-mm-mrad directly after the extraction system. We also showed emittance scans at the end of the non-ideal LEBT. The large emittance growth in the LEBT can be attributed to the strong multipole components in the dipole fringe fields. Borrowed equipment was used to assemble the test stand. Furthermore, the dipole magnet has no vertical focusing, and a pair of quadrupole magnets were used to compensate for this. However, the agreement between simulation and measurement is quite good, and we are working on further improving our model.

Contamination of the source with heavier-mass species in a previous commissioning run was significantly reduced by replacing a pair of O-rings and a cracked ceramic insulator. Once the source has warmed up, contaminants are virtually non-existent. The source

FIG. 16. Log–log plot of the mean free path of H_2^+ with respect to collisions with neutral H_2. Cross section data from IAEA's ALADDIN database.[38] An error of $\pm30\%$ based on cross section and pressure errors is plotted as a band.

now operates stably over periods of several hours without significant changes in the beam current and composition.

As a final point of discussion, we would like to mention that the stainless steel body of the source, while robust, turned out not to be ideal in terms of transferring heat away through the water cooling channels. Particularly, the plasma aperture showed distortions after long running times (several hours) at high power in early measurements. We replaced it with a 75% tungsten, 25% copper alloy. We are beginning to replace other source parts with a high yield-strength copper alloy such as *Elmedur*.

V. OUTLOOK AND CONCLUSION

We have presented a new filament-driven multicusp ion source, designed to produce high currents of H_2^+ in DC mode for long-time operation, and established simulations that are in good agreement with the constructed device. We reported a maximum current of 1.42 mA from a 4 mm aperture consisting of 76% H_2^+, which corresponds to a current of 1.08 mA of H_2^+ and a maximum current of 2.05 mA consisting of 62% H_2^+, which corresponds to a current of 1.3 mA of H_2^+. To our knowledge, these are the highest H_2^+ currents published to date from a multicusp ion source in DC mode, while H_2^+ was the dominant species. This is an important milestone for MIST-1, and as described below, we have a clear path for further improvement.

In addition to the construction of the source, we developed an accurate simulation model of the ion source and beamline, which was compared with mass spectra and emittance measurements in DB2 with good agreement. Thus, although the LEBT itself has certain shortcomings (due to the use of borrowed equipment), we understand the beam dynamics well and can estimate the beam quality directly after the source from the measurements at the end of the LEBT. This is corroborated by emittance measurements of the total beam (> 70% H_2^+) in DB1. The emittance after extraction is <0.05 π-mm-mrad (rms, normalized) at 0.95 mA total extracted current, which meets the IsoDAR requirements.

For the novel RFQ direct injection method that we are proposing for the IsoDAR experiment,[3,40,41] the nominal goal is 10 mA of H_2^+ delivered by the ion source. If we scale our 4 mm diameter aperture results up to an 8 mm aperture (assuming constant plasma density), we should theoretically be able to deliver 5 mA of H_2^+ while maintaining an emittance of <0.1 π-mm-mrad. We confirmed this scaling with IBSimu simulations of small variations around a total current density of 12 mA/cm^2 with 4 and 8 mm apertures (see Fig. 18). Note that the emittances for the 4 mm case are lower than the measured 0.05 π-mm-mrad. This is due to the fact that during the measurements, we used a higher-than-ideal source voltage, which improves LEBT transmission at the expense of emittance increase (extraction simulations with a higher source voltage show the expected higher emittance).

This is only a factor of 2 short of the goal. With the ongoing systematic tests of filament material, shape, and position as well as a stronger magnetic confinement field, the available H_2^+ beam current will be significantly increased. Furthermore, improved cooling will allow higher discharge currents, also leading to higher plasma densities and, thus, higher currents. Even with the currently reachable 5 mA of H_2^+, a compact cyclotron of the IsoDAR design could be built that delivers five times more proton current (assuming 50%
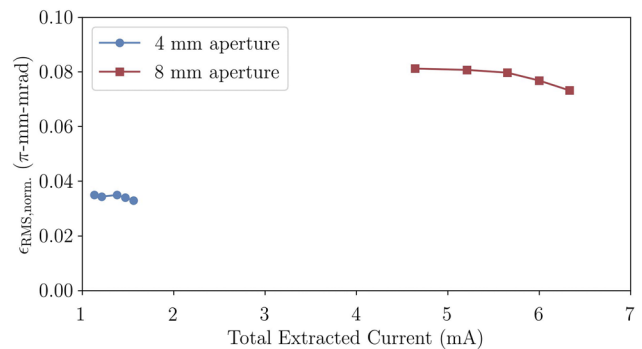

FIG. 18. Simulated emittances for beam extraction from a 4 mm and an 8 mm aperture compared side-by-side. We observe that the 8 mm aperture results still show an emittance below the required 0.1π-mm-mrad (rms, normalized). The decreasing emittance with a higher current indicates that the extraction voltage is still too high for optimal beam formation at the meniscus.

losses during injection, 2.5 mA of H_2^+ corresponds to 5 mA of protons after charge-stripping) than commercially available machines and also exceeds record holder PSI Injector II, which delivers a maximum of 2.7 mA protons.[42]

AUTHOR DECLARATIONS
Conflict of Interest

The authors have no conflicts to disclose.

DATA AVAILABILITY

The data that support the findings of this study are available from the corresponding author upon reasonable request.

REFERENCES

[1]A. Bungau, A. Adelmann, J. R. Alonso, W. Barletta, R. Barlow, L. Calabretta, A. Calanna, D. Campo, J. M. Conrad, Z. Djurcic, Y. Kamyshkov, M. H. Shaevitz, I. Shimizu, T. Smidt, J. Spitz, M. Wascko, L. A. Winslow, and J. J. Yang, Phys. Rev. Lett. **109**, 141802 (2012).

[2]M. Abs, A. Adelmann, J. R. Alonso, S. Axani, W. A. Barletta, R. Barlow, L. Bartoszek, A. Bungau, L. Calabretta, A. Calanna, D. Campo, G. Castro, L. Celona, G. H. Collin, J. M. Conrad, S. Gammino, R. Johnson, G. Karagiorgi, S. Kayser, W. Kleeven, A. Kolano, F. Labrecque, W. A. Loinaz, J. Minervini, M. H. Moulai, H. Okuno, H. Owen, V. Papavassiliou, M. H. Shaevitz, I. Shimizu, T. M. Shokair, K. F. Sorensen, J. Spitz, M. Toups, M. Vagins, K. Van Bibber, M. O. Wascko, D. Winklehner, L. A. Winslow, and J. J. Yang, arXiv:1511.05130 [hep-ex, physics:physics] (2015).

[3] D. Winklehner, J. Bahng, L. Calabretta, A. Calanna, A. Chakrabarti, J. Conrad, G. D'Agostino, S. Dechoudhury, V. Naik, L. Waites, and P. Weigel, Nucl. Instrum. Methods Phys. Res., Sect. A **907**, 231 (2018), part of Special Issue: Honour of Kai Siegbahn.

[4] J. R. Alonso, R. Barlow, J. M. Conrad, and L. H. Waites, Nat. Rev. Phys. **1**, 533–535 (2019).

[5] L. H. Waites, J. R. Alonsom, R. Barlow, and J. M. Conrad, EJNMMI Radiopharm. Chem. **5**, 6 (2020).

[6] Y. Ishi, M. Inoue, Y. Kuriyama, Y. Mori, T. Uesugi, J. Lagrange, T. Planche, M. Takashima, E. Yamakawa, H. Imazu et al., in Proceedings of IPAC10 (JACoW, Kyoto, 2010), p. 1323.

[7] K. Inoue, Int. J. Mod. Phys. A **19**, 1157 (2004).

[8] A. Bungau, J. Alonso, L. Bartoszek, J. Conrad, M. Shaevitz, and J. Spitz, J. Instrum. **14**(03), P03001 (2019).

[9] A. Bungau, J. Alonso, L. Bartoszek, J. M. Conrad, E. Dunton, and M. H. Shaevitz, J. Instrum. **15**(07), T07002 (2020).

[10] W. Wu, S. Peng, T. Ma, H. Ren, J. Zhang, T. Zhang, Y. Jiang, K. Li, Y. Xu, A. Zhang, J. Wen, Z. Guo, and J. Chen, Rev. Sci. Instrum. **90**, 101501 (2019).

[11] R. Miracoli, L. Celona, G. Castro, D. Mascali, S. Gammino, D. Lanaia, R. Di Giugno, T. Serafino, and G. Ciavola, Rev. Sci. Instrum. **83**, 02A305 (2012).

[12] Y. Xu, S. Peng, H. Ren, J. Zhao, J. Chen, A. Zhang, T. Zhang, Z. Guo, and J. Chen, Rev. Sci. Instrum. **85**, 02A943 (2013).

[13] W. Schweizer, U. Ratzinger, B. Klump, and K. Volk, Rev. Sci. Instrum. **85**, 02A743 (2014).

[14] K. W. Ehlers and K. N. Leung, Rev. Sci. Instrum. **54**, 677 (1983).

[15] G. Castro, D. Mascali, L. Celona, S. Gammino, C. Caliri, F. Di Bartolo, D. Lanaia, M. Mazzaglia, R. Miracoli, L. Neri et al., Rev. Sci. Instrum. **85**, 096109 (2014).

[16] G. Castro, G. Torrisi, L. Celona, D. Mascali, L. Neri, G. Sorbello, O. Leonardi, G. Patti, G. Castorina, and S. Gammino, Rev. Sci. Instrum. **87**, 083303 (2016).

[17] J. R. Alonso, L. Calabretta, D. Campo, L. Celona, J. Conrad, R. G. Martinez, R. Johnson, F. Labrecque, M. H. Toups, D. Winklehner, and L. Winslow, Rev. Sci. Instrum. **85**, 02A742 (2014).

[18] J. Alonso, S. Axani, L. Calabretta, D. Campo, L. Celona, J. M. Conrad, A. Day, G. Castro, F. Labrecque, and D. Winklehner, J. Instrum. **10**(10), T10003 (2015).

[19] N. Joshi, M. Droba, O. Meusel, and U. Ratzinger, Nucl. Instrum. Methods Phys. Res., Sect. A **606**, 310 (2009).

[20] D. Wutte, S. Freedman, R. Gough, Y. Lee, M. Leitner, K. N. Leung, C. Lyneis, D. S. Pickard, M. D. Williams, and Z. Q. Xie, Nucl. Instrum. Methods Phys. Res., Sect. B **142**, 409 (1998).

[21] Y. Lee, R. A. Gough, W. B. Kunkel, K. N. Leung, L. T. Perkins, D. S. Pickard, L. Sun, J. Vujic, M. D. Williams, and D. Wutte, Nucl. Instrum. Methods Phys. Res., Sect. B **119**, 543 (1996).

[22] S. Axani, D. Winklehner, J. Alonso, and J. M. Conrad, Rev. Sci. Instrum. **87**, 02B704 (2016).

[23] J. Komppula and O. Tarvainen, Plasma Sources Sci. Technol. **24**, 045008 (2015).

[24] R. Celiberto, R. K. Janev, A. Laricchiuta, M. Capitelli, J. M. Wadehra, and D. E. Atems, At. Data Nucl. Data Tables **77**, 161 (2001).

[25] T. Kalvas, O. Tarvainen, T. Ropponen, O. Steczkiewicz, J. Ärje, and H. Clark, Rev. Sci. Instrum. **81**, 02B703 (2010).

[26] P. W. Allison, J. D. Sherman, and D. B. Holtkamp, IEEE Trans. Nucl. Sci. **30**, 2204 (1983).

[27] J. Corona, "An emittance scanner for high-intensity, low-energy ion beams," Senior thesis, Massachusetts Institute of Technology, 2018.

[28] P. Avery, "Introduction to PID control," https://www.machinedesign.com/automation-iiot/sensors/article/21831887/introduction-to-pid-control, 2020.

[29] A. Friedman, R. H. Cohen, D. P. Grote, S. M. Lund, W. M. Sharp, J.-L. Vay, I. Haber, and R. A. Kishek, IEEE Trans. Plasma Sci. **42**, 1321 (2014).

[30] See http://warp.lbl.gov/ for Warp, 2021.

[31] S. Nishioka, S. Abe, S. Mattei, J. Lallement, T. Kalvas, A. Hatayama, and J. Lettry, AIP Conf. Proc. **2011**(1), 080017 (2018).

[32] T. Kalvas, O. Tarvainen, J. Komppula, H. Koivisto, J. Tuunanen, D. Potkins, T. Stewart, and M. Dehnel, AIP Conf. Proc. **1655**(1), 030015 (2015).

[33] V. Toivanen, T. Kalvas, H. Koivisto, J. Komppula, and O. Tarvainen, J. Instrum. **8**(05), P05003 (2013).

[34] O. Midttun, Y. Levinsen, R. Miyamoto, and C. Plostinar, in 8th International Particle Accelerator Conference (IPAC'17), Copenhagen, Denmark, 14–19 May 2017, http://www.jacow.org, pp. 4445–4447.

[35] M. Reiser, Theory and Design of Charged Particle Beams, 2nd ed. (Wiley-VCH, Weinheim, 2008).

[36] D. Winklehner and D. Leitner, J. Instrum. **10**(10), T10006 (2015).

[37] See https://www.comsol.com/ for COMSOL: Multiphysics software for optimizing designs, 2020.

[38] See https://www-amdis.iaea.org/ALADDIN/ for IAEA AMDIS ALADDIN Database, 2021.

[39] W. Yang, S. N. Averkin, A. V. Khrabrov, I. D. Kaganovich, Y.-N. Wang, S. Aleiferis, and P. Svarnas, Phys. Plasmas **25**, 113509 (2018).

[40] D. Winklehner, R. Hamm, J. Alonso, and J. Conrad, in 6th International Particle Accelerator Conference (IPAC2015), 2015.

[41] D. Winklehner, R. Hamm, J. Alonso, J. M. Conrad, and S. Axani, Rev. Sci. Instrum. **87**, 02B929 (2016).

[42] M. Seidel, S. Adam, A. Adelmann, C. Baumgarten, Y. Bi, R. Doelling, H. Fitze, A. Fuchs, M. Humbel, J. Grillenberger et al., in Proceedings of the 1st International Particle Accelerator Conference (JACoW, 2010), p. 1309.